Received: 11 October 2022 | Revised: 10 July 2023 | Accepted: 4 September 2023

DOI: 10.1002/cnm.3772

APPLIED RESEARCH

WILEY

Computational modeling of low-density lipoprotein accumulation at the carotid artery bifurcation after stenting

Nasrul H. Johari[1,2] | **Claudia Menichini**[1] | **Mohamad Hamady**[3] | **Xiao Y. Xu**[1]

[1]Department of Chemical Engineering, Imperial College London, South Kensington Campus, London, UK

[2]Centre for Advanced Industrial Technology, University Malaysia Pahang, Pekan, Pahang, Malaysia

[3]Department of Surgery & Cancer, Imperial College London, St. Mary's Campus, London, UK

Correspondence
Nasrul H. Johari, Department of Chemical Engineering, Imperial College London, South Kensington Campus, London, UK.
Email: nhadi@ump.edu.my

Funding information
Fundamental Research Grant Scheme (FRGS), Grant/Award Numbers: RDU210109, FRGS/1/2021/TK0/UMP/02/8; Imperial College London for the PhD scholarship

Abstract

Restenosis typically occurs in regions of low and oscillating wall shear stress, which also favor the accumulation of atherogenic macromolecules such as low-density lipoprotein (LDL). This study aims to evaluate LDL transport and accumulation at the carotid artery bifurcation following carotid artery stenting (CAS) by means of computational simulation. The computational model consists of coupled blood flow and LDL transport, with the latter being modeled as a dilute substance dissolved in the blood and transported by the flow through a convection-diffusion transport equation. The endothelial layer was assumed to be permeable to LDL, and the hydraulic conductivity of LDL was shear-dependent. Anatomically realistic geometric models of the carotid bifurcation were built based on pre- and post-stent computed tomography (CT) scans. The influence of stent design was investigated by virtually deploying two different types of stents (open- and closed-cell stents) into the same carotid bifurcation model. Predicted LDL concentrations were compared between the post-stent carotid models and the relatively normal contralateral model reconstructed from patient-specific CT images. Our results show elevated LDL concentration in the distal section of the stent in all post-stent models, where LDL concentration is 20 times higher than that in the contralateral carotid. Compared with the open-cell stents, the closed-cell stents have larger areas exposed to high LDL concentration, suggesting an increased risk of stent restenosis. This computational approach is readily applicable to multiple patient studies and, once fully validated against follow-up data, it can help elucidate the role of stent strut design in the development of in-stent restenosis after CAS.

KEYWORDS

carotid artery stenting, low-density lipoprotein, stent design

1 | INTRODUCTION

In recent years, the number of patients requiring carotid artery stenting (CAS) has increased compared to carotid artery endarterectomy (CAE). This is due to the nature of CAS treatment, which is less invasive, has a shorter recovery time, and is recommended to patients with high-risk surgery complications.[1,2] However, this treatment faces challenges of late failure resulting from long-term patency and restenosis[3]

Results from clinical trials on the long-term follow-up of CAS reported in-stent restenosis (ISR) rates ranging from 5.0 to 17.3%.[2–5] Data pertaining to the incidence of restenosis have shown the influence of stent characteristics with different designs and configurations.[6,7] Previous studies reported different risks of peri-procedural incidents in patients treated with open-cell stents and closed-cell stents.[6,8,9]

The stent designs and vessel geometry correlate strongly with neointimal hyperplasia regions, modulated by wall shear stress.[10–12] Differences in stent design may contribute to the disparity in wall shear stress distribution and subsequent development of neointimal hyperplasia; the latter involves platelet aggregation, smooth muscle cell proliferation and migration, and accumulation of inflammatory cells and fatty deposits. Several studies used wall shear stress as a hemodynamic risk indicator to identify potential regions of ISR[10,12,13] and to determine the optimal stent type for specific vessels. They found that post-stent models with a closed-cell type had a larger area of low and oscillating wall shear stress compared to the open-cell type. Similarly, Hussain et al.[9] collected clinical data that showed restenosis was higher in patients with closed-cell stents over a follow-up period of 20.2 ± 16.4 months. This finding was supported by Texakalidis et al.[14] that open-cell stents were associated with a lower risk of restenosis compared to closed-cell stents.

It is well known that the initiation and progression of atherosclerosis are directly associated with a high level of low-density lipoprotein (LDL) accumulation in the arterial wall.[15–18] The high incidence of coronary atherosclerosis has led to numerous studies of hemodynamics and LDL transport in the coronary artery,[19–31] demonstrating high LDL concentration in regions prone to atherosclerotic plaque formation. LDL accumulation is also suggested to promote plaque formation in the aorta[32–34] and carotid artery.[35–38] In the case of restenosis, recent reports suggest that the process starts with neoatherosclerosis after stenting, characterized by the accumulation of lipid-laden foamy macrophages within the neointimal layer.[39–42] Therefore, early accumulation of LDL could be the most crucial reason for intimal thickening, which is the first step of arterial narrowing (initiation of intimal thickening).

Different models of LDL transport through an arterial wall have been proposed in the literature.[43] The simplest model is the wall-free model, where only the fluid domain is considered in the simulation, and the effects of the surrounding wall are incorporated through the imposed boundary conditions.[34,44,45] Coupled fluid-wall models where the wall is treated as a single layer of homogenous porous medium wall have been developed to investigate macromolecule transport, including oxygen and LDL transport in arteries.[46–48] A more realistic wall model using an anatomically realistic multi-layered structure has also been proposed to model mass transport within the wall.[49] Another advanced model combining a multi-layered wall with a multi-pore model for mass transfer of LDL has been applied to a stenosed coronary artery[27] and has shown improved prediction of LDL concentration in the local proximity of the endothelium, particularly for the initial progress of atherosclerosis.

Following these advancements, several computational models of atherosclerosis have been investigated by different research groups in order to characterize the onset of the disease.[19,24,50,51] However, computational studies on the mass transport of macromolecules in post-stenting arteries are still lacking. Few studies have examined the altered hemodynamics caused by different post-stent geometry on neointimal hyperplasia (NIH).[42] Understanding the effects of detailed stent cell geometry on the accumulation of atherogenic macromolecules such as LDL is essential for further future improvement and optimization of stent design. Modeling mass transport phenomena would also help elucidate the role of stent design and vascular curvature[52] in LDL clearance near the endothelial surface.

In order to investigate how the different stent designs could affect the transport of biologically active molecules dissolved in the blood, LDL transport was simulated in three post-stent carotid artery bifurcation models and a healthy contralateral carotid bifurcation, with the latter being used as a control. LDL transport was described using a convection-diffusion model accounting for trans-endothelial transport.

2 | MODELS AND METHODS

2.1 | Reconstruction of the carotid artery bifurcation and stents

A patient with asymptomatic chronic stenosis (90% according to NASCET grading) in the right internal carotid artery (ICA) was examined using contrast-enhanced computed tomography angiography (CTA). Due to the patient medical background, the patient was recommended for endovascular intervention using CAS. Figure 1 shows a self-expanding Wallstent (Carotid WALLSTENT 6–8 × 37 mm, Boston Scientific, MA) deployed in the ICA and distal to the common carotid artery (CCA). According to the NHS Health Research Authority guidelines and regulations to the guidelines and regulations of the NHS Health Research Authority in England, formal ethical approval was not required for this limited retrospective and anonymized study.

The post-stent CTA images were acquired to reconstruct patient-specific models. The images were acquired using Philips Ingenuity CT machine with a slightly lower resolution: 100 slices of the carotid artery were taken with a thickness of 2 mm for each slice, interslice of 1 mm and pixel size of .549 mm with a higher dose of 120 kV and 67.99 mAs. Two carotid bifurcation geometric models were built: (a) the post-stent model (reconstructed from post-stent CTA images of the right carotid) and (b) the contralateral carotid with low-grade stenosis (30%), reconstructed from CTA images of the left carotid. Both geometries were reconstructed with approximately similar dimensions—for CCA, the diameter is within .8 to 1.0 cm with the length of 7.0 to 7.2 cm. Similarly, for ICA length from the apex of bifurcation to the end is ∼6.2 to 6.5 cm. However, the diameter of the geometries differed in the area of distal and proximal to the bifurcation, that is, 1.12 cm is the largest diameter in the post-stent model compared with .81 cm in the contralateral model. The post-stent model is larger than the contralateral model primarily due to the deployed stent shape. Another factor is the existence of low-grade stenosis in the contralateral model at the bulb area wall. The ICA length for both models was built way longer than the external carotid artery (ECA) as the region of interest for the flow pattern analysis comparison.

The reconstruction process begins with the segmentation of the inner surface of the carotid artery based on thresholding values and region-growing technique using MIMICS 16.0 (Materialise Inc., Leuven, Belgium). The sequence began with marking the region of interest, which was the lumen of the CCA, ICA, and ECA in the transverse plane. The region of interest was highlighted using pixel intensity, and the same procedure was repeated to all transverse plane images. The surface contours were then highlighted pixels and the smoothing criteria. The smoothing was done based on the prescribed measures to ensure the accuracy of the surface contours. Then, the 3D surface was created by superimposing and lofting these surface contours in the coronal plane, representing the 3D geometry of patient-

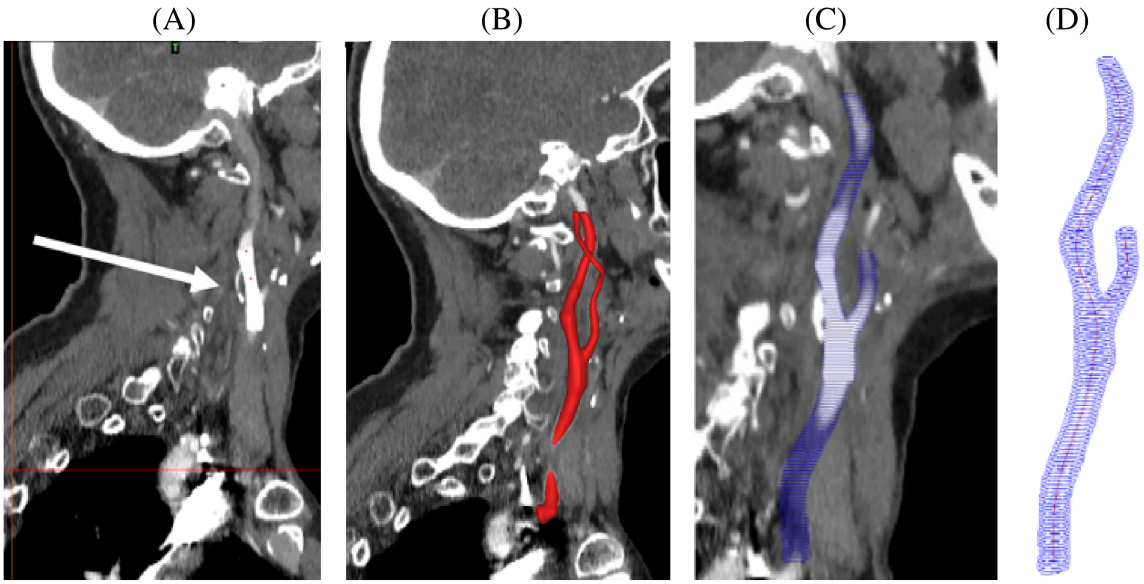

FIGURE 1 (A) CT image of post-stent carotid artery bifurcation showing metallic artifact due to the presence of stent metal. (B) Volume rendering and segmentation of the model from CT images before generation (C) polylines. (D) Both polylines and centerlines were exported to CAD files to reconstruct the lumen surface.

specific carotid artery bifurcation. The smoothing level was controlled to ensure that none of the important physiological features were lost during the smoothing process. Polylines of the segmented post-stent geometry were also created together with the centerline path before being exported to SolidWorks (Dassault Systemes, Velizy, France) for lofting.

For stents creation in Figure 2, a generic approach to reconstruct the deployed stent was developed by making use of the following information: (1) geometry of the post-stent carotid bifurcation and (2) stent-specific properties including the number and width of cells, circumferential and longitudinal struts, as well as the overall stent length and diameter. To virtually deploy the stent, a series of Boolean operations were performed. Firstly, the stented region was separated from the post-stent model to undergo virtual stenting. The region was then wrapped with the parameterized sketch of the stent cell and hollowed to .12 mm thickness. An intersection Boolean operation was performed between the stent cell geometry and the stented region in order to remove the vessel and isolate the stent geometry. The stent geometry was then exported into a reconstructed post-stent carotid bifurcation. Lastly, a patient-specific stented carotid bifurcation model was obtained by subtracting the stent geometry from the post-stent model and removing the strut volume from the flow domain at the opening of the ECA. The inclusion of the stent struts at the opening of ECA is important in order to assess the effect of stent design and location on post-stent carotid hemodynamics. To investigate the influence of open- and closed-cell stent designs on blood flow patterns, models of two additional commercial stent designs were built. Stent B was created to represent another closed-cell stent design resembling an XACT stent, and Stent C was created for an open-cell design to resemble an ACCULINK stent (Figure 3).

The models were then exported and discretized into tetrahedral elements using ANSYS ICEM CFD 15.0. Initially, the 'octree' method was used before the volume mesh was regenerated using the 'delaunay' method to ensure the high-quality unstructured mesh. The skewness of the mesh elements and the mesh expansion factor were kept as small as possible. Figure 4 shows the mesh elements generated with local refinement around the stent struts, where the mesh density was much greater than in the rest of the model. A finer mesh strategy, including gradually finer elements toward the wall, was used to ensure convergence of the near wall transport equations and appropriate spatial resolution for LDL flux in the endothelial layer.[54] Hence, the number of mesh elements increased by 15% more than the ones reported in our previous study.[53] Mesh sensitivity tests were carried out for both models to ensure mesh-independent solutions. The final meshes for all post-stent models are approximately 8.2 million elements, while the contralateral model consists of approximately 3 million elements.

2.2 | Flow and LDL transport modeling

Laminar and pulsatile blood flows were simulated by numerically solving the governing equations for an incompressible fluid using a finite volume-based CFD code (ANSYS CFX 15.0). Blood was treated as incompressible and non-

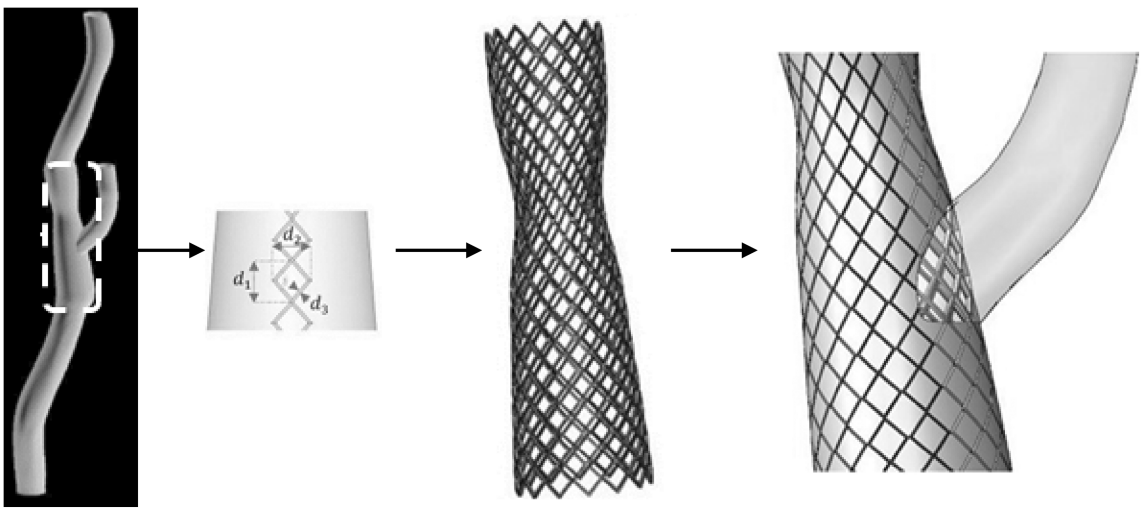

FIGURE 2 (from left to right) The stented area in the dotted square is wrapped with a parameterized sketch of stent cells. Using Boolean operation, the intersection of the stent cells and solid surface yields the realistic expanded Wallstent before subtracting it from the post-stent model to create a stented carotid artery bifurcation model (post-stent model) for CFD simulation.

FIGURE 3 Three stent designs geometries in the deployed configuration. (From left) WALLSTENT, XACT (Stent B), and Acculink (Stent C). Figure adapted from the previous study.[53]

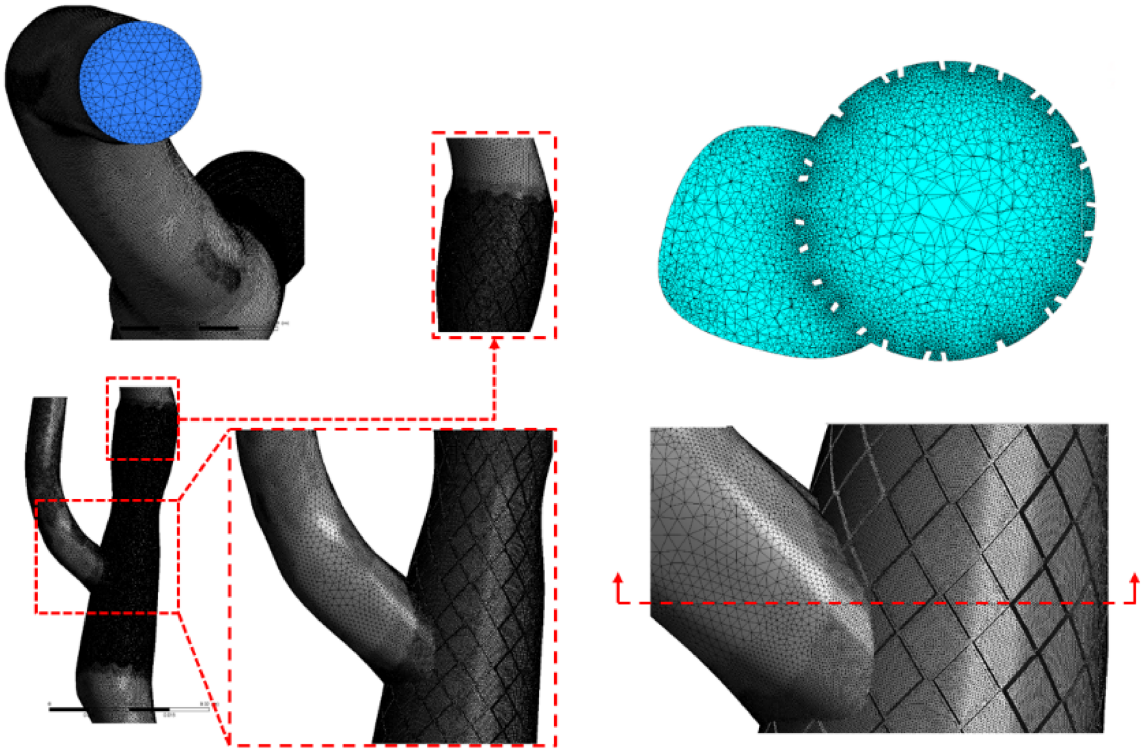

FIGURE 4 The tetrahedral elements mesh used in the post-stent carotid bifurcation model with high-density concentration in the stented region, especially in the vicinity of stent struts.

Newtonian with a density of 1060 kg/m^3, while its viscosity was described using the Quemada model.[55] The Quemada viscosity model was adapted to incorporate regions of high shear rate with more than 100 s^{-1} with regions of stagnation, especially at the stent struts. The Quemada is appropriate for capturing the variability of viscosity characteristics at the low end of shear rates.[55] In order to obtain clinically relevant numerical results, accurate boundary conditions need to be specified at the CCA inlet and the ICA and ECA outlets. For this purpose, Womersley[56] velocity profiles were applied at the CCA inlet, which was derived from the corresponding mean velocity waveforms of Doppler ultrasound. An instantaneous mean velocity (i.e., averaged across the Doppler beam) of a cardiac cycle was extracted for the

calculation of the inlet flow rate by multiplying it with the cross-sectional area of the inlet CCA measured with CTA (Figure 5). Through the Womersleys method obtained using Matlab (Mathworks, Natick, MA), a harmonic patient-specific fully developed time-varying velocity profile was then specified at the CCA inlet.

Physiological pressure outflow boundary conditions were obtained using the 3-element Windkessel model (3-EWM). The 3-EWM has been proven to provide numerical results closer to in vivo, where the resistance of the downstream vasculature and arterial compliance determine the pressure at the outlet. The first resistance, R_1 is the proximal resistance which depends on the outlet diameter, C is the total wall compliance of the downstream vasculature, and R_2 is the distal resistance offered by the peripheral resistance of the vessel. Pressures and flowrates at each ICA and ECA outlets are related by the following Ordinary Differential Equation (ODE)[57];

$$Q_{out,ICA}\left(1+\frac{R_{1,ICA}}{R_{2,ICA}}\right)+C_{ICA}R_{1,ICA}\frac{dQ_{out,ICA}}{dt}=C_{ICA}\frac{dP_{out,ICA}}{dt}+\frac{P_{out,ICA}}{R_{2,ICA}}, \tag{1}$$

$$Q_{out,ECA}\left(1+\frac{R_{1,ECA}}{R_{2,ECA}}\right)+C_{ECA}R_{1,ECA}\frac{dQ_{out,ECA}}{dt}=C_{ECA}\frac{dP_{out,ECA}}{dt}+\frac{P_{out,ECA}}{R_{2,ECA}}, \tag{2}$$

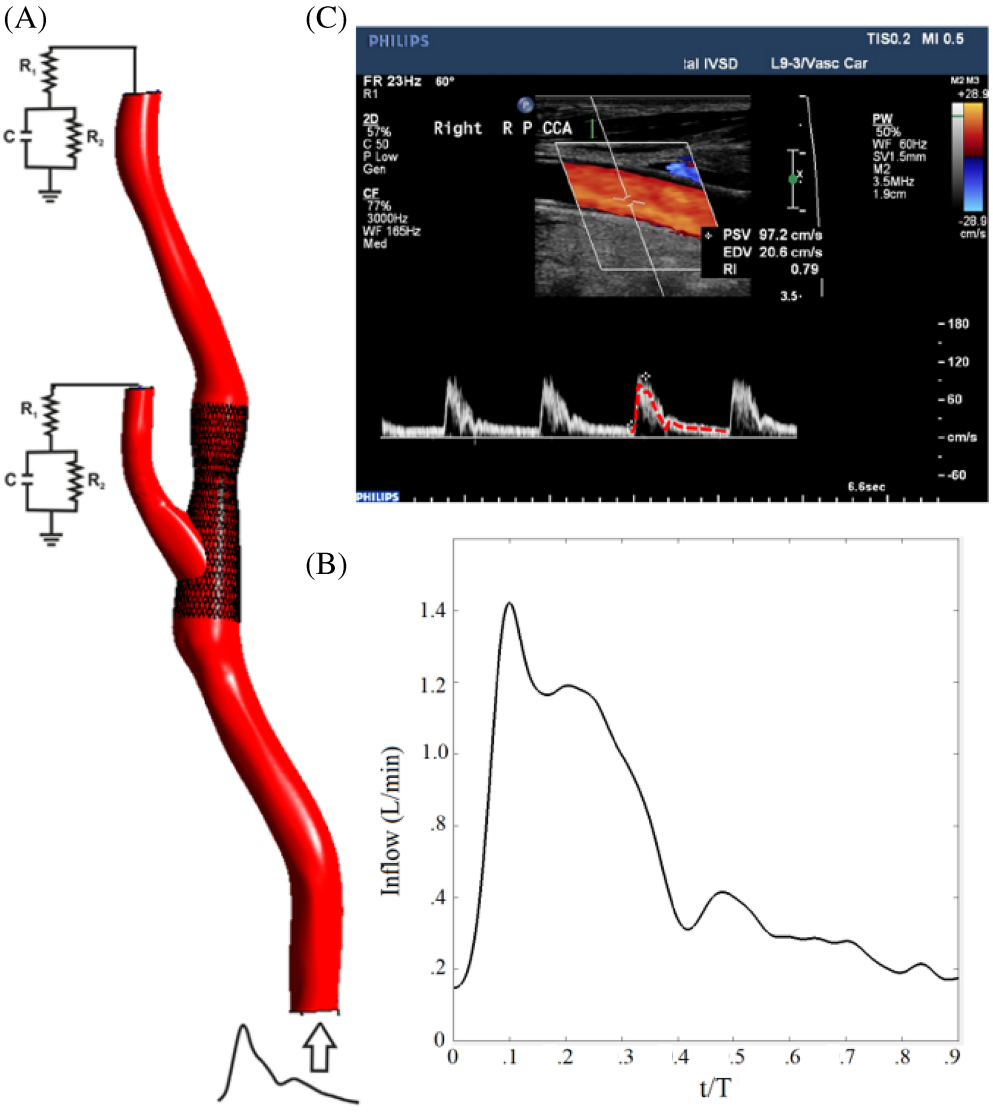

FIGURE 5 Schematic of the computational model employed in this study is similar to our previous report.[53] (A) The carotid bifurcation model together with the RCR network model at the ECA and ICA outlets and (B) the inflow waveform prescribed at the CCA inlet section based on (C) Doppler ultrasound measurements.

TABLE 1 Windkessel parameters for each outlet.

Model	Boundary	R_1 (Pa s/m^3)	R_2 (Pa s/m^3)	C (m^3/Pa)
Post-stent	ICA	4.107×10^8	2.924×10^9	5.757×10^{-10}
	ECA	6.707×10^8	5.099×10^9	3.327×10^{-10}
Pre-stent	ICA	7.944×10^8	9.742×10^9	1.822×10^{-10}
	ECA	1.001×10^8	1.633×10^9	7.288×10^{-10}
Contralateral	ICA	8.969×10^8	2.756×10^9	5.255×10^{-10}
	ECA	7.292×10^8	4.074×10^9	3.977×10^{-10}

where Q_{out} is the outlet flowrate that can be calculated from the Doppler ultrasound velocity waveform, while C, R_1, and R_2 were fitted parameters and adjusted to match the maximum, minimum and cycle-averaged carotid blood pressures of 110, 90 and 70 mmHg, respectively (Table 1). Different values for these parameters were calculated for the contralateral and post-stent models based on the corresponding measured flow waveforms at the outlets. The walls were assumed to be rigid with no-slip conditions.

LDL was modeled as a dilute substance dissolved in the blood and transported by the flow through a convection-diffusion transport equation:

$$\frac{\partial c}{\partial t} + u \cdot \nabla c = D\nabla^2 c, \tag{3}$$

where c is LDL concentration, u is blood velocity vector, and D is LDL diffusivity in blood. A physiological concentration of 1.2 mg/mL was applied at the inlet.[34] The endothelial layer was assumed to be permeable to LDL, with LDL flux (Js) and transmural velocity (J_v) being described by the Kedem-Katchalsky equations:

$$J_s = k_w \Delta c + J_v\left(1-\sigma_f\right)\overline{c}, \tag{4}$$

$$J_v = L_p\left(\Delta P - \sigma_D \Delta \prod\right), \tag{5}$$

where L_p is the hydraulic conductivity of the endothelium, ΔP is the pressure drop across the arterial wall, $\Delta\prod$ is the oncotic pressure difference, σ_D and σ_f are respectively the osmotic and solvent reflection coefficients, k_w is the LDL endothelial permeability, Δc is the LDL concentration difference across the endothelial wall and $\overline{c}$ is the average endothelial concentration.[58] The shear-dependent equation for hydraulic conductivity L_p proposed by Sun et al.[23] was adopted in order to incorporate the influence of local shear stress τ_w on transmural flux:

$$L_p(|\tau_w|) = .392 \times 10^{-12} \ln(|\tau_w| + .015) + 2.7931 \times 10^{-12}. \tag{6}$$

All parameter values have been taken from Sun et al.[23] In order to account for the early effects of smooth muscle cell proliferation, the strut thickness was reduced to half of its original size in the three post-stent models.

It is well known that the time scale of LDL transport is much greater than a cardiac cycle. In other words, LDL accumulation in atheroprone regions would take months or years to form. Within the current limitations of computational power, it is only feasible to simulate a limited number of cardiac cycles under pulsatile flow. While it is possible to observe differences in spatial distribution of LDL on the endothelial and sub-endothelial surfaces, it would be desirable to predict LDL accumulation over a longer time period. Clearly, simulating LDL accumulation over months/years in a real-time scale would be computationally prohibitive. This difficulty was circumvented by artificially accelerating the near wall processes. This artificial acceleration was achieved by multiplying the LDL flux by an enhancement coefficient, ϕ, which is related to the local time-averaged shear rate:

$$\phi = 10^{4\frac{\gamma_t^5}{\gamma_t^5+\gamma_{av}^5}}, \tag{7}$$

where γ_{av} is the time-averaged shear rate and γ_t is a pre-defined threshold value for shear rate. The coefficient will be equal to 1 in regions where the local time-averaged shear stress is greater than .4 (i.e., $\gamma_{av} >> \gamma_t = 37\,s^{-1}$ for Quemada viscosity model), and it will be equal to 10^4 in regions of particularly low shear. The .4 value is based on Malek et al.[59] that suggested the wall area with TAWSS <.4 Pa is considered to be atheroprone, in which atherosclerotic lesions co-localize with regions of low wall shear stress. In regions where the local time-averaged shear stress is below .4 Pa, the wall flux will be enhanced by 10^4-fold, so that LDL accumulation over a much longer time scale can be predicted by only simulating a few cardiac cycles:

$$\phi\left(J_v c - D\frac{\partial c}{\partial n}\bigg|_{wall}\right) = \phi J_s \tag{8}$$

This methodology allows us to de-couple the time scales of solute and blood transport, simulating a wall transport process occurring over a time scale of the order of 10^4 s (~3 h) per cardiac cycle.

2.3 | Computational details

In ANSYS CFX 15.0, a high-resolution advection strategy was utilized to spatially discretize the Navier–Stokes equation, while a second order implicit backward Euler scheme was employed to temporally discretize the equation. The model was first to run for three cardiac cycles to get a periodic flow solution and to initialize the model variables. Then the LDL model was included starting with the fourth cardiac cycle. For temporal advancement, a uniform time-step of .001 s was employed, with a maximum root-mean-square (RMS) residual of 10^{-5} manually specified to regulate the solution's precision. Around 15–20 iterations were required to attain convergence at each time step. Overall, CFD simulations including the LDL transport simulations for all post-stent models, require an average of 3 h of computer processing time per cardiac cycle using an Intel Xeon E5-2697 workstation with 24 cores and 96 GB RAM.

3 | RESULTS AND DISCUSSION

Figure 6 shows the local sub-endothelial LDL concentration with normal near-wall transport in the four models. For the contralateral carotid (Figure 6A), the normalized LDL concentration is concentrated around the bifurcation wall, especially at the outer wall of CCA to ICA. Elevated LDL concentrations of about 3.4% are observed in this area which is the entrance of the carotid bulb. The increase of LDL in this area was reported earlier by Kenjeres and Loor,[60] with a maximum increase of 3.5% in the healthy patient-specific carotid bifurcation model. The variation of LDL concentration distribution can be interpreted through observation of time-averaged wall shear stress (TAWSS) gradients. As reported in References 38,53,60, low TAWSS corresponds to the recirculation flow structure within the carotid bulb. The area of high LDL concentration is limited to the connection of CCA and ICA, which corresponds to the area of low TAWSS in the geometry. The computed area for both low TAWSS and high LDL is similar to Kim and Giddens,[38] who applied realistic wall thickness to represent wall structure in their FSI simulations. The local flow fields are highly dependent upon individual or patient-specific lumen and wall geometry as well as the blood flowrates, thus making the reconstruction of actual hemodynamic environment is crucial since the wall shear stress is used as the basis to measure local LDL transport parameters.

To establish additional correlations between the local flow and LDL concentration distributions, an arbitrarily selected '0 to 1' line profile along the lumen wall of the carotid bulb is extracted (Figure 7A). The resulting profiles of TAWSS and normalized LDL concentration along the '0 to 1' line are plotted the Figure 7B for comparison. It can be seen that a local minimum of the TAWSS takes place at $L/L_o = .2$ before gradually increasing toward the end of the profile line. At the same location, profiles of normalized LDL concentration reached local maximum and gradually decreased, respectively. This means that many areas with low WSS also have high LDL concentrations along the

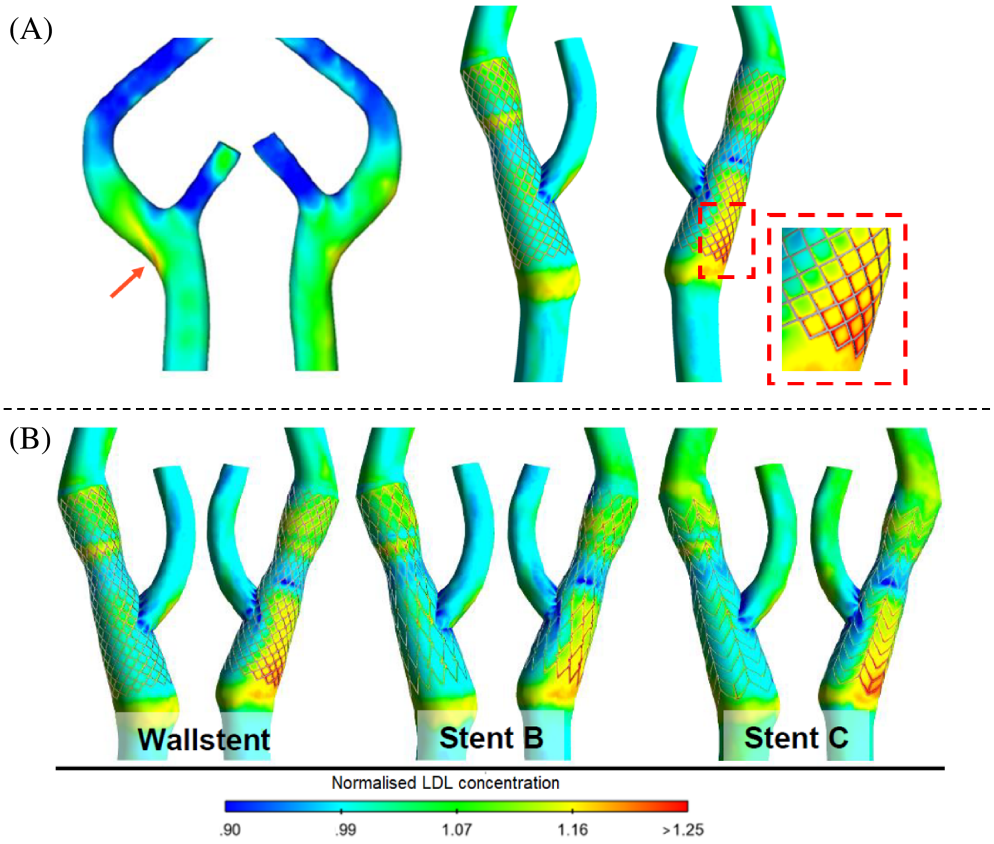

FIGURE 6 Sub-endothelial LDL concentration in the post-stent models and in the contralateral carotid obtained with normal wall transport. (A) Comparison between the contralateral carotid and the Wallstent carotid showing the exact location of high concentration of LDL accumulation, (B) all three different post-stent models showing similar pattern of high LDL accumulation distribution at the proximal region.

endothelium layer. Similar findings were also recorded in References 44,60 where the area of lowest WSS and highest LDL concentration mostly coincide.

For the post-stent models, elevated LDL concentrations are observed in the proximal portion of the stent along the outer wall, especially at the sharp corners of the struts, with less pronounced LDL accumulation in the distal region (Figure 6A). The highest normalized concentration found in these regions is up to 2.34, about 80% higher than the contralateral carotid. The elevated LDL concentration was observed around the stent struts in all post-stent models, with the highest LDL is at the outer wall of CCA to ICA. As the geometry shapes of the post-stent models are identical, the spatial pattern of LDL is observed following the stent design. A marginally larger area of elevated LDL concentration occurs in the Wallstent model compared to the other two models (Figure 6B). Since the geometrical feature of the Wallstent has a higher number of stent cells, it causes a larger area of complex flow patterns near the wall, especially between the struts. Similar to the contralateral model, these areas are dominantly covered by low TAWSS which directly correspond to local flow recirculation close to the struts (Figure 8). This abnormal hemodynamic environment leads to larger areas of low TAWSS. Similar results were also recorded by Santis et al.[13] in the study of restenosis prediction using wall shear stress and indices computed from CFD simulations on ideal open- and closed-cell stents.

The LDL concentrations in the contralateral carotid are not affected by the artificial acceleration of its near wall transport as shown in Figure 9. A similar location of elevated LDL concentrations is recorded in the carotid bulb. However, the accelerated LDL concentration in the contralateral model may not be compared directly with previous studies. Kenjeres and Loor[60] used steady laminar flow profile with identical Re = 105, while Kim and Giddens[38] only performed simulations in three cardiac cycles. However, all post-stent models observed notable changes in accelerated LDL concentrations. First, there is a substantial increase in LDL accumulation in different regions of the stented geometries where concentrations are more than 20 times higher than in the contralateral carotid. Second, LDL accumulation is most pronounced in the distal region of the stent, with Stent C showing the least coverage of high LDL hot spots.

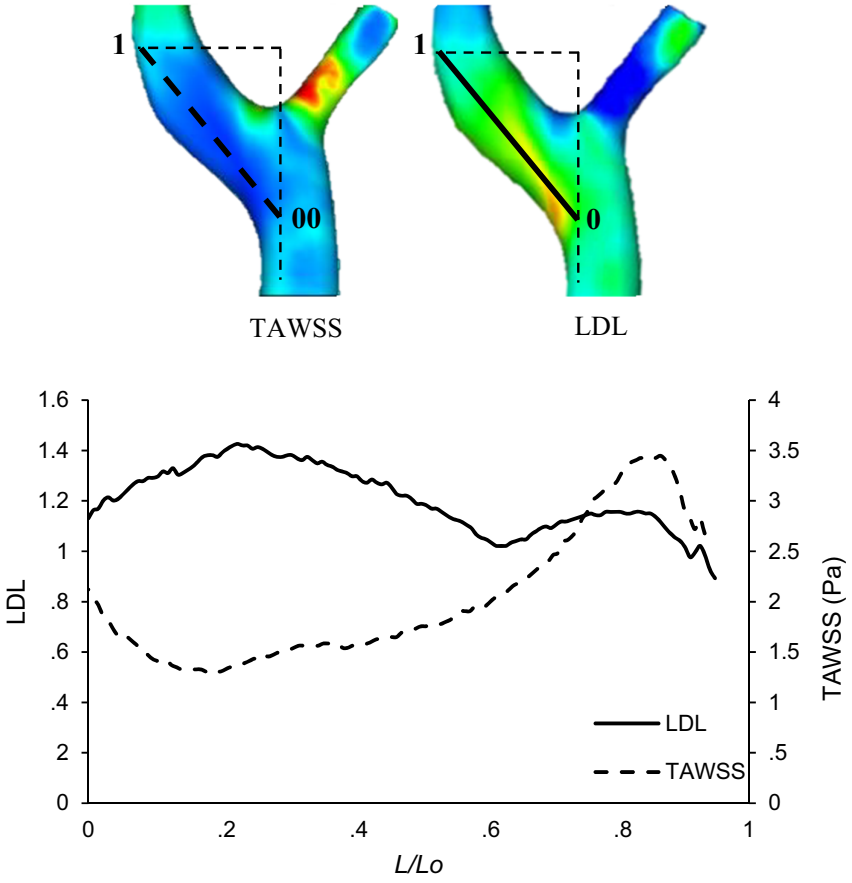

FIGURE 7 (A) The contours of normalized LDL concentration and TAWSS at the bifurcation area and location of the lines (L/L_0) for extraction of the characteristic profiles. (B) The profiles along the L/L_0 lines compare LDL concentration and TAWSS (Pa).

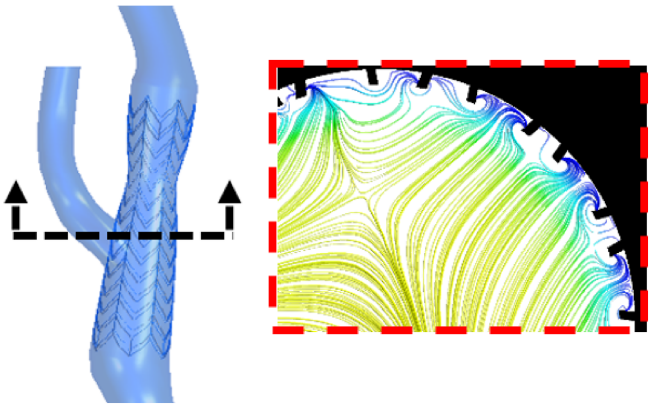

FIGURE 8 Recirculation flows in free cell area between the stent struts. This figure has been reported in the previous study by our group.[53]

Finally, LDL accumulation in the proximal region only occurs at a few isolated spots. According to previous studies, restenosis occurs mostly within the first year after CAS,[61,62] and the accelerated near-wall transport simulation is indeed useful to approach realistic LDL accumulation duration.

While LDL concentrations in the contralateral carotid are not affected by the artificial acceleration of its near-wall transport, obvious changes are noted for the post-stent models. Significant LDL accumulation toward the distal end of the stent could be attributed to the combined effect of bending at both ends of the stent, slightly enlarged local diameter, and a mild constriction in the middle of the stent. Isolated spots of LDL accumulation were also observed at the

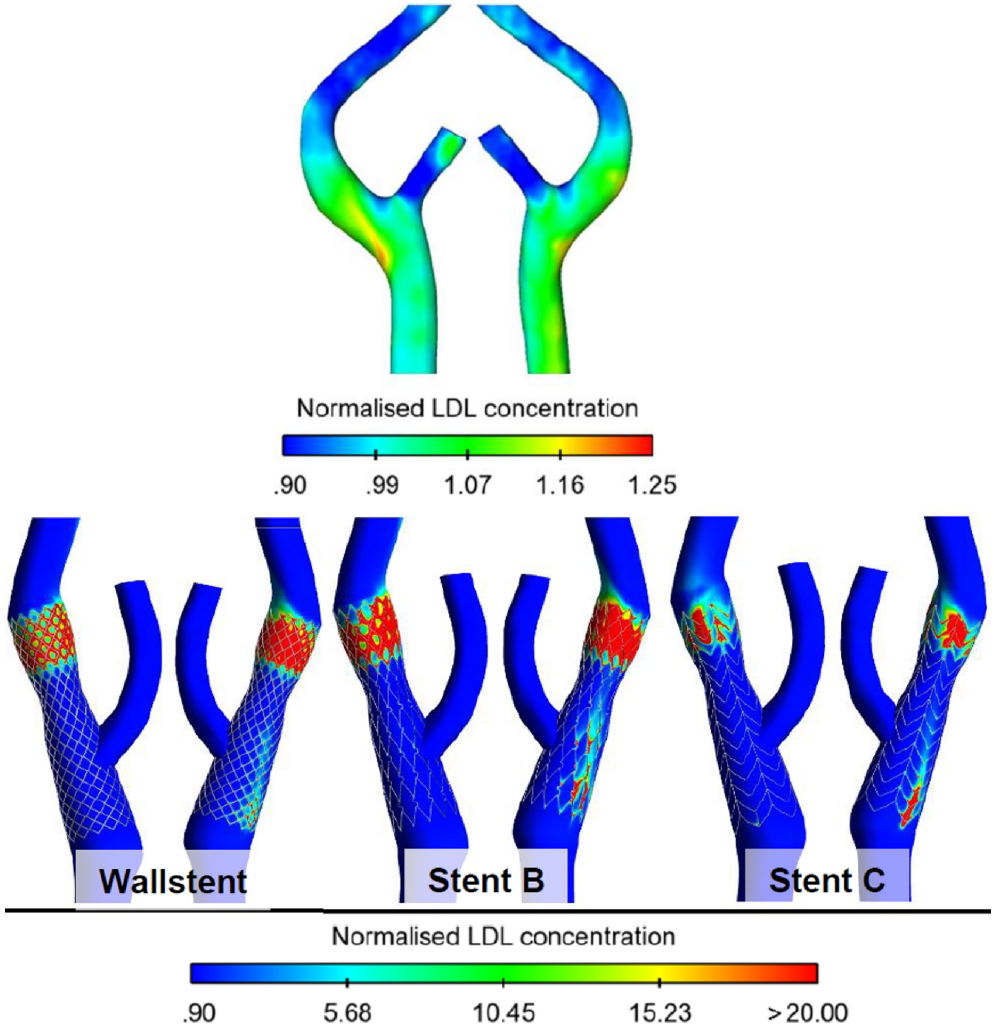

FIGURE 9 LDL concentrations in the contralateral carotid (top) and the post-stent carotids (bottom) obtained with accelerated near-wall transport.

proximal end of the stent, but these were limited to the sharp corners around the struts. Based on our results, LDL accumulation appeared to be more pronounced in Wallstent and Stent B—both are closed-cell stents. Nonetheless, it should be borne in mind that our simulation results were based on the assumption that the plaque was pushed back uniformly by the stent so that any possible protrusion of the plaque through the free cell area of the stent was not taken into account.

The methodology presented in this study allows us to replicate stent apposition from the post-CAS patient-specific geometry, maintaining the complex shape of the stent struts such as floating struts at the ECA entrance and a small constriction downstream of the bifurcation; all of these influence the local hemodynamics.[4,5] The results clearly show that the patient-specific geometry and stent design in post-stent models affects the distribution of LDL concentration. Low endothelial shear stress, flow recirculation, and stagnation are known to be associated with weak convective clearance near the endothelial surface, which could result in local accumulation of biologically active compounds like LDL.[28,63] Through artificial acceleration of the near wall processes, we were able to simulate LDL accumulation over a much longer time period than a few cardiac cycles. Using a low TAWSS threshold of .4 Pa to trigger the accelerated transport,[59] our computational results predicted a potential risk for LDL accumulation in the distal segment of the stent in all post-stent models, although the coverage of LDL accumulation was less in Stent C (open-cell).

Figure 10 shows a comparison of local hemodynamic features, that is, TAWSS, oscillatory shear index (OSI) and relative residence time (RRT) reported in Johari et al.'s Reference 53, with LDL accumulation in the least potential risk of ISR model, Stent C. As blood flow may change its direction, many studies have used OSI to quantify the cyclic motion,

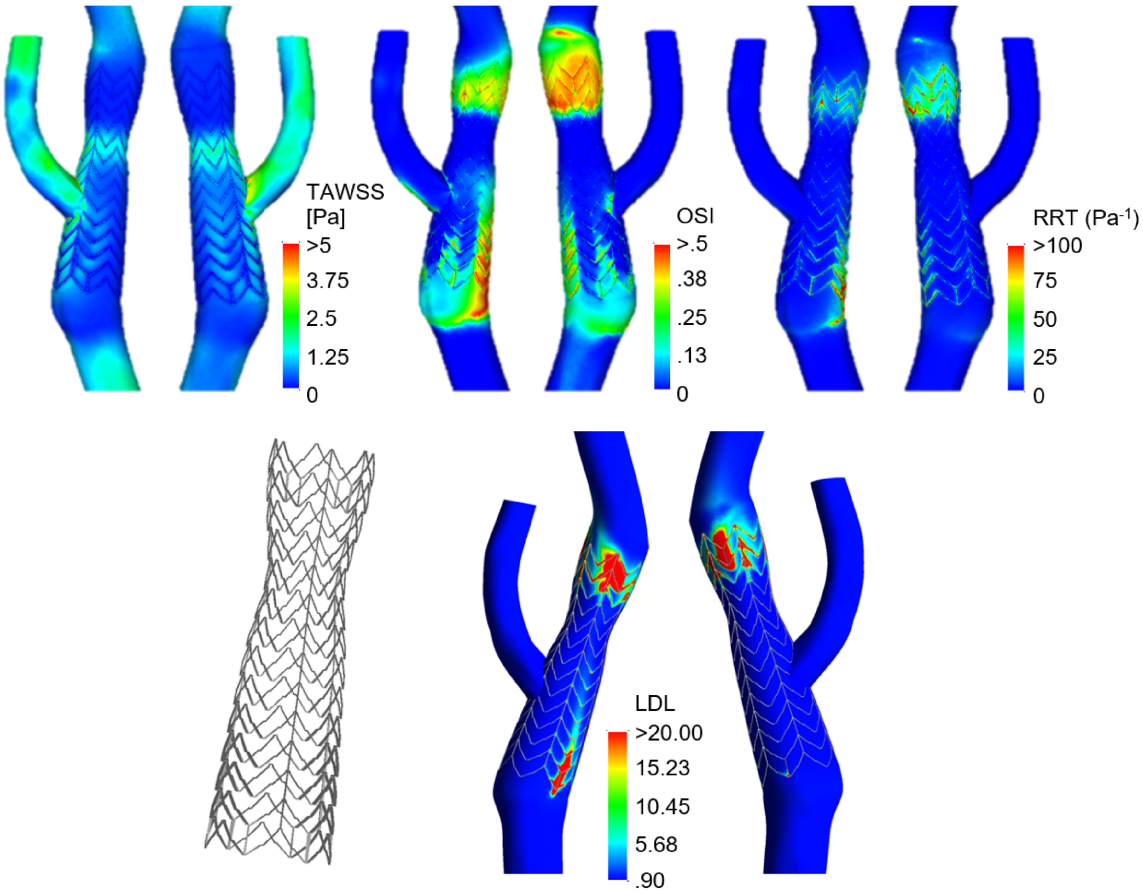

FIGURE 10 Comparison of hemodynamic simulations (top) reported by Johari et al. 2020[53] with LDL concentrations in post-stent model, Stent C (bottom).

ranging between 0 and a maximum .5. RRT predicts the likelihood of cell deposition on the arterial wall.[64] Low TAWSS, elevated OSI, and high RRT have been reported being correlated with neointimal thickening, which could potentially lead to ISR. The LDL simulation presented in this study revealed the same spots of high LDL concentration with the hemodynamic features, especially at the area toward the distal end of the stent. The unfavorable hemodynamic features and LDL accumulation in post-stent models were consistent with Texakalidis et al.,[14] who found that open-cell stents were associated with a statistically lower risk of restenosis compared to closed-cell stents.

By artificially accelerating the wall transport process, this study has demonstrated the feasibility of simulating LDL accumulation in the wall over a much longer timescale than several cardiac cycles. Since the buildup of LDL is involved in the initial stage of intimal thickening, the current findings can be used to predict the risk of intimal thickening based on the distribution of LDL accumulation in the carotid artery.

This method can be applied to multiple patient cases to elucidate further stent design's role in the development of ISR after CAS. There are four limitations of this study. First, the model for LDL transport was limited to luminal and trans-endothelium transport without accounting for the multi-layered structure of the arterial wall. The initial condition of LDL concentration was also assumed with a constant value ($C{=}C_0$), proving by a previous study[65] that different LDL concentrations may produce different patterns of LDL distributions in the artery. However, the present study aims to compare the LDL distribution between different stent designs with the normal contralateral carotid. The purpose is to identify which stent design is predicted to have a higher risk of stent restenosis. Hence, we believe our initial condition of constant LDL concentration profiles diluted in blood flow is reasonable to meet the study's purpose. Nonetheless, the recommendation by Reference 65 is beneficial for future studies.

Second, the vessel wall and the stent were assumed to be rigid in the CFD simulations; nevertheless, as the study aimed to observe the pattern of LDL distribution in the stented region, the rigid wall assumption is expected to have a minor influence on the results.[66] To account for the potential influence of remodeling on the hemodynamics, the strut thickness was also reduced to half of its original size in all post-stent models. This adjustment attempts to partially

consider the remodeling of the stent's geometry and its effects on the flow patterns and LDL distribution. The findings reported by Corti et al.[67] are in line with the assumptions made in the current study regarding stent remodeling. They observed that most of the restenosis occurred in the first post-operative month, and subsequent remodeling affected the hemodynamics, leading to a slowing down of the restenosis process over time. While the current study did not explicitly simulate the long-term follow-up and remodeling process as performed by Corti et al.,[67] the inclusion of the stent strut thickness reduction aimed to consider the potential effects of remodeling on the results. However, it is important to note that the specific influence of remodeling on the results was not extensively investigated in the current study.

It would be more interesting to evaluate the qualitative comparison of LDL concentration between the different sizes of the stenotic model (pre-stent) and post-stent models. The absence of follow-up data has limited the study for any direct comparison between the predicted LDL accumulation and restenosis, especially the LDL concentration values around the stent strut. A few previous articles simulated the LDL transport in the other parts of the stented artery, such as Gai et al.,[68] Liu et al.,[69] and Escuer et al.[70] However, none of the articles proposed the LDL concentration values in the stented area. Nonetheless, the similarity of the three articles is that the normalized LDL concentration around the stent struts is way higher than in the other endothelium wall, which is also predicted in the present study. The studies are not focusing on the stent strut shape and size, as they mentioned difficulties in reproducing the complex geometry of the stent; hence, the simplified circular stent area was employed in the study. Besides, the clinical observation study by[68] recommends further analysis for possible LDL concentration values in the specific stent area. Finally, regarding the influence of different acceleration factors on the areas of high LDL concentration, it is to note that the specific influence of other acceleration factors was not addressed in this particular study. Instead, the focus was on assessing LDL influx in a longer time period and providing preliminary results. Further evaluation and validation of the computational technique used in this study, including performing sensitivity analyses with different acceleration factors would be useful in the future studies for a more comprehensive understanding of the model's behavior.

4 | CONCLUSION

In this study, we investigated the accumulation of LDL in patient-specific post-stent carotid bifurcation models reconstructed from CTA images to predict the potential of restenosis. The predicted LDL accumulation was compared between the closed- and open-cell stents models and the normal contralateral model. Our results clearly show that LDL accumulation is more pronounced in Wallstent and Stent B—both are closed-cell stents. This computational technique is readily applicable to various patient data. Once fully validated against follow-up data, it can help elucidate the role of stent strut design in the development of in-stent restenosis after CAS. Future studies of more patient-specific models using our methodology will be beneficial to assess the impact of more stent designs and vessel curvatures, especially with specific post-stenting follow-up information. This will facilitate a similar analysis to determine key factors in the progression of restenosis.

ACKNOWLEDGMENTS

Nasrul H. Johari gratefully acknowledges support from the Government of Malaysia for the PhD scholarship award and the Ministry of Higher Education for providing financial support under the Fundamental Research Grant Scheme (FRGS) No. FRGS/1/2021/TK0/UMP/02/8 (University reference RDU210109). Claudia Menichini gratefully acknowledges the support of Imperial College London for the PhD scholarship.

DATA AVAILABILITY STATEMENT

The data that support the findings of this study are available from the corresponding author upon reasonable request.

ORCID

Nasrul H. Johari https://orcid.org/0000-0003-2297-3463

REFERENCES

1. Cole TS, Mezher AW, Catapano JS, et al. Nationwide trends in carotid endarterectomy and carotid artery stenting in the post-CREST era. *Stroke*. 2020;51:579-587. doi:10.1161/STROKEAHA.119.027388
2. Brott TG, Calvet D, Howard G, et al. Long-term outcomes of stenting and endarterectomy for symptomatic carotid stenosis: a preplanned pooled analysis of individual patient data. *Lancet Neurol*. 2019;18(4):348-356. doi:10.1016/S1474-4422(19)30028-6

3. Bonati LH, Gregson J, Dobson J, et al. Restenosis and risk of stroke after stenting or endarterectomy for symptomatic carotid stenosis in the international carotid stenting study (ICSS): secondary analysis of a randomised trial. *Lancet Neurol*. 2018;17(7):587-596. doi:10.1016/S1474-4422(18)30195-9
4. Moon K, Albuquerque FC, Levitt MR, Ahmed AS, Kalani MYS, McDougall CG. The myth of restenosis after carotid angioplasty and stenting. *J Neurointerv Surg*. 2016;8(10):1006-1010. doi:10.1136/neurintsurg-2015-011938
5. Mas JL, Arquizan C, Calvet D, et al. Long-term follow-up study of endarterectomy versus angioplasty in patients with symptomatic severe carotid stenosis trial. *Stroke*. 2014;45(9):2750-2756. doi:10.1161/STROKEAHA.114.005671
6. Alparslan B, Nas OF, Eritmen UT, Duran S, Ozkaya G, Hakyemez B. The effect of stent cell geometry on carotid stenting outcomes. *Cardiovasc Intervent Radiol*. 2016;39(4):507-513. doi:10.1007/s00270-015-1211-3
7. Timaran CH, Rosero EB, Higuera A, Ilarraza A, Modrall JG, Clagett GP. Randomized clinical trial of open-cell vs closed-cell stents for carotid stenting and effects of stent design on cerebral embolization. *J Vasc Surg*. 2011;54(5):1310-1316.e1.
8. Muller MD, Gregson J, McCabe DJH. Stent design, restenosis and recurrent stroke after carotid artery stenting in the international carotid stenting study. *J Vasc Surg*. 2020;71(2):713. doi:10.1016/j.jvs.2019.11.006
9. Hussain HG, Aparajita R, Khan SZ, Rezayat C, McKinsey JF, Dayal R. Closed-cell stents present with higher velocities on duplex ultrasound compared with open-cell stents after carotid intervention: short- and mid-term results. *Ann Vasc Surg*. 2011;25(1):55-63. doi:10.1016/j.avsg.2010.07.004
10. Yao X, Dai Z, Zhang X, et al. Carotid geometry as a predictor of in-stent neointimal hyperplasia: a computational fluid dynamics study. *Circ J*. 2019;83(7):1472-1479. doi:10.1253/circj.CJ-18-1152
11. Conti M, Long C, Marconi M, Berchiolli R, Bazilevs Y, Reali A. Carotid artery hemodynamics before and after stenting: a patient specific CFD study. *Comput Fluids*. 2016;141:62-74. doi:10.1016/j.compfluid.2016.04.006
12. Gundert TJ, Marsden AL, Yang W, Ladisa JF. Optimization of cardiovascular stent design using computational fluid dynamics. *J Biomech Eng*. 2012;134(1):1-8. doi:10.1115/1.4005542
13. De Santis G, Trachet B, Conti M, et al. A computational study of the hemodynamic impact of open- versus closed-cell stent design in carotid artery stenting. *Artif Organs*. 2013;37(7):E96-E106. doi:10.1111/aor.12046
14. Texakalidis P, Giannopoulos S, Kokkinidis DG, Lanzino G. Effect of open- vs closed-cell stent design on periprocedural outcomes and restenosis after carotid artery stenting: a systematic review and comprehensive meta-analysis. *J Endovasc Ther*. 2018;25(4):523-533. doi:10.1177/1526602818783505
15. Ference BA, Ginsberg HN, Graham I, et al. Low-density lipoproteins cause atherosclerotic cardiovascular disease. 1. Evidence from genetic, epidemiologic, and clinical studies. A consensus statement from the European atherosclerosis society consensus panel. *Eur Heart J*. 2017;38(32):2459-2472. doi:10.1093/eurheartj/ehx144
16. Wadhera RK, Steen DL, Khan I, Giugliano RP, Foody JM. A review of low-density lipoprotein cholesterol, treatment strategies, and its impact on cardiovascular disease morbidity and mortality. *J Clin Lipidol*. 2016;10(3):472-489. doi:10.1016/j.jacl.2015.11.010
17. Tomkin GH, Owens D. LDL as a cause of atherosclerosis. *J Atheroscler Thromb*. 2012;5(1):13-21. doi:10.2174/1876506801205010013
18. Mitra S, Goyal T, Mehta JL. Oxidized LDL, LOX-1 and atherosclerosis. *Cardiovasc Drugs Ther*. 2011;25(5):419-429. doi:10.1007/s10557-011-6341-5
19. Sakellarios AI, Tsompou P, Kigka V, et al. Non-invasive prediction of site-specific coronary atherosclerotic plaque progression using lipidomics, blood flow, and LDL transport modeling. *Appl Sci*. 1976;2021(11):1-14.
20. Piemjaiswang R, Ding Y, Feng Y, Piumsomboon P, Chalermsinsuwan B. Effect of transport parameters on atherosclerotic lesion growth: a parameter sensitivity analysis. *Comput Methods Prog Biomed*. 2021;199:105904. doi:10.1016/j.cmpb.2020.105904
21. Siogkas P, Sakellarios A, Exarchos TP, et al. Multiscale – patient-specific artery and atherogenesis models. *IEEE Trans Biomed Eng*. 2011;58:3464-3468. doi:10.1109/TBME.2011.2164919
22. Olgac U, Poulikakos D, Saur SC, Alkadhi H, Kurtcuoglu V. Patient-specific three-dimensional simulation of LDL accumulation in a human left coronary artery in its healthy and atherosclerotic states. *Am J Physiol Heart Circ Physiol*. 2009;296(6):H1969-H1982. doi:10.1152/ajpheart.01182.2008
23. Sun N, Torii R, Wood NB, Hughes AD, Thom SAM, Xu XY. Computational modeling of LDL and albumin transport in an in vivo CT image-based human right coronary artery. *J Biomech Eng*. 2009;131(2):1-9. doi:10.1115/1.3005161
24. Chen X, Zhuang J, Huang H, Wu Y. Fluid – structure interactions (FSI) based study of low – density lipoproteins (LDL) uptake in the left coronary artery. *Sci Rep*. 2021;11(4803):1-12. doi:10.1038/s41598-021-84155-3
25. Pleouras D, Sakellarios AI, Kyriakidis S, et al. A computational multi-level atherosclerotic plaque growth model for coronary arteries. *Proceedings of the Annual International Conference of the IEEE Engineering in Medicine and Biology Society, EMBS*. Vol 2019. IEEE; 2019:5010-5013. doi:10.1109/EMBC.2019.8857329
26. Abbasian M, Shams M, Valizadeh Z, Moshfegh A, Javadzadegan A, Cheng S. Effects of different non-Newtonian models on unsteady blood flow hemodynamics in patient-specific arterial models with in-vivo validation. *Comput Methods Prog Biomed*. 2020;186:105185. doi:10.1016/j.cmpb.2019.105185
27. Kenjereš S, van der Krieke JP, Li C. Endothelium resolving simulations of wall shear-stress dependent mass transfer of LDL in diseased coronary arteries. *Comput Biol Med*. 2019;114:103453. doi:10.1016/j.compbiomed.2019.103453
28. Sakellarios A, Bourantas CV, Papadopoulou SL, et al. Prediction of atherosclerotic disease progression using LDL transportmodelling: a serial computed tomographic coronary angiographic study. *Eur Heart J Cardiovasc Imaging*. 2017;18(1):11-18. doi:10.1093/ehjci/jew035

29. Sakellarios AI, Räber L, Bourantas CV, et al. Prediction of atherosclerotic plaque development in an In vivo coronary arterial segment based on a multilevel modeling approach. *IEEE Trans Biomed Eng*. 2017;64(8):1721-1730. doi:10.1109/TBME.2016.2619489
30. Nouri M, Jalali F, Karimi G, Zarrabi K. Image-based computational simulation of sub-endothelial LDL accumulation in a human right coronary artery. *Comput Biol Med*. 2015;62:206-221. doi:10.1016/j.compbiomed.2015.04.013
31. Sakellarios AI, Papafaklis MI, Siogkas P, et al. Patient-specific computational modeling of subendothelial LDL accumulation in a stenosed right coronary artery: effect of hemodynamic and biological factors. *Am J Physiol Heart Circ Physiol*. 2013;304(11):H1455-H1470. doi:10.1152/ajpheart.00539.2012
32. Soltany Sadrabadi M, Hedayat M, Borazjani I, Arzani A. Fluid-structure coupled biotransport processes in aortic valve disease. *J Biomech*. 2021;117:117. doi:10.1016/j.jbiomech.2021.110239
33. Mpairaktaris DG, Soulis JV, Giannoglou GD. Low density lipoprotein transport through patient-specific thoracic arterial wall. *Comput Biol Med*. 2017;89(July):115-126. doi:10.1016/j.compbiomed.2017.07.025
34. Lantz J, Karlsson M. Large eddy simulation of LDL surface concentration in a subject specific human aorta. *J Biomech*. 2012;45(3):537-542. doi:10.1016/j.jbiomech.2011.11.039
35. Nagargoje M, Gupta R. Effect of sinus size and position on hemodynamics during pulsatile flow in a carotid artery bifurcation. *Comput Methods Prog Biomed*. 2020;192:105440. doi:10.1016/j.cmpb.2020.105440
36. Sakellarios AI, Bizopoulos P, Papafaklis MI, et al. Natural history of carotid atherosclerosis in relation to the hemodynamic environment: a low-density lipoprotein transport modeling study with serial magnetic resonance imaging in humans. *Angiology*. 2017;68(2):109-118. doi:10.1177/0003319716644138
37. Kenjereš S. On recent Progress in modelling and simulations of multi-scale transfer of mass, momentum and particles in bio-medical applications. *Flow Turbul Combust*. 2016;96(3):837-860. doi:10.1007/s10494-015-9669-2
38. Kim S, Giddens DP. Mass transport of low density lipoprotein in reconstructed hemodynamic environments of human carotid arteries: the role of volume and solute flux through the endothelium. *J Biomech Eng*. 2015;137(4):041007. doi:10.1115/1.4028969
39. Meng L, Liu X, Yu H, et al. Incidence and predictors of neoatherosclerosis in patients with early in-stent restenosis determined using optical coherence tomography. *Int Heart J*. 2020;61(5):872-878. doi:10.1536/ihj.20-139
40. Hasegawa S, Nakano T, Mukai Y, et al. High low-density lipoprotein cholesterol as an independent risk factor for coronary restenosis in hemodialysis patients undergoing percutaneous coronary interventions. *Ther Apher Dial*. 2021;25(3):296-303. doi:10.1111/1744-9987.13558
41. Wu Y, Fu X. Comprehensive analysis of predictive factors for rapid angiographic stenotic progression and restenosis risk in coronary artery disease patients underwent percutaneous coronary intervention with drug-eluting stents implantation. *J Clin Lab Anal*. 2019;33(2):1-13. doi:10.1002/jcla.22666
42. Dai Z, Xu G. Restenosis after carotid artery stenting. *Vascular*. 2017;25(6):576-586. doi:10.1177/1708538117706273
43. Corti A, Colombo M, De Nisco G, Rodriguez Matas JF, Migliavacca F, Chiastra C. Computational investigation of the role of low-density lipoprotein and oxygen transport in atherosclerotic arteries. *Modeling of Mass Transport Processes in Biological Media*. Elsevier; 2022:139-213. doi:10.1016/b978-0-323-85740-6.00017-0
44. Wada S, Karino T. Computational study on LDL transfer from flowing blood to arterial walls. *Clinical Application of Computational Mechanics to the Cardiovascular System*. Springer; 2000:157-173. doi:10.1007/978-4-431-67921-9_16
45. Soulis JV, Fytanidis DK, Papaioannou VC, Giannoglou GD. Wall shear stress on LDL accumulation in human RCAs. *Med Eng Phys*. 2010;32(8):867-877. doi:10.1016/j.medengphy.2010.05.011
46. Stangeby DK, Ethier CR. Coupled computational analysis of arterial LDLtransport- effects of hypertension. *Comput Methods Biomech Biomed Engin*. 2002;5(3):233-241. doi:10.1080/10255840290010733
47. Stangeby DK, Ethier CR. Computational analysis of coupled blood-wall arterial LDL transport. *J Biomech Eng*. 2002;124(1):1-8. doi:10.1115/1.1427041
48. Moore JA, Ethier CR. Oxygen mass transfer calculations in large arteries. *J Biomech Eng*. 1997;119(4):469-475. doi:10.1115/1.2798295
49. Yang N, Vafai K. Modeling of low-density lipoprotein (LDL) transport in the artery-effects of hypertension. *Int J Heat Mass Transf*. 2006;49(5–6):850-867. doi:10.1016/j.ijheatmasstransfer.2005.09.019
50. Pignani A, Di Venuta I, Boghi A, Gori F. Mass transfer and blood flow in a patient-specific three-dimensional Willis circle. *Int Commun Heat Mass Transf*. 2021;126(May):105369. doi:10.1016/j.icheatmasstransfer.2021.105369
51. Johari NH, Wood NB, Cheng Z, et al. Disturbed flow in a stenosed carotid artery bifurcation: comparison of RANS-based transitional model and les with experimental measurements. *Int J Appl Mech*. 2019;11(4):1-21. doi:10.1142/S1758825119500327
52. Tarbell JM. Mass transport in arteries and the localization of atherosclerosis. *Annu Rev Biomed Eng*. 2003;5:79-118. doi:10.1146/annurev.bioeng.5.040202.121529
53. Johari NH, Hamady M, Xu XY. A computational study of the effect of stent design on local hemodynamic factors at the carotid artery bifurcation. *Artery Res*. 2020;26(3):161-169. doi:10.2991/artres.k.200603.001
54. Tada S. Numerical study of oxygen transport in a carotid. *Phys Med Biol*. 2010;55(14):3993-4010. doi:10.1088/0031-9155/55/14/004
55. Quemada D. Rheology of concentrated disperse systems II. A model for non-newtonian shear viscosity in steady flows. *Rheol Acta*. 1978;17(6):632-642. doi:10.1007/BF01522036
56. Womersley J. Method for calculation of velocity, rate of flow and viscous drag in arteries when the pressure gradient is known. *J Physiol*. 1955;127(3):553-563.

57. Xiao N, Alastruey J, Figueroa CA. A systematic comparison between 1-D and 3-D hemodynamics in compliant arterial models. *Int J Numer Meth Biomed Engng*. 2014;30:204-231. doi:10.1002/cnm
58. Sun N, Wood NB, Hughes AD, Thom SAM, Xu XY. Influence of pulsatile flow on LDL transport in the arterial wall. *Ann Biomed Eng*. 2007;35(10):1782-1790. doi:10.1007/s10439-007-9347-1
59. Malek AM, Alper SL. Hemodynamic shear stress and and its role in a therosclerosis. *JAMA*. 1999;282(21):2035-2042. doi:10.1001/jama.282.21.2035
60. Kenjereš S, De Loor A. Modelling and simulation of low-density lipoprotein transport through multi-layered wall of an anatomically realistic carotid artery bifurcation. *J R Soc Interface*. 2014;11(91):20130941. doi:10.1098/rsif.2013.0941
61. Wasser K, Schnaudigel S, Wohlfahrt J, et al. Clinical impact and predictors of carotid artery in-stent restenosis. *J Neurol*. 2012;259(9):1896-1902. doi:10.1007/s00415-012-6436-3
62. Gröschel K, Riecker A, Schulz JB, Ernemann U, Kastrup A. Systematic review of early recurrent stenosis after carotid angioplasty and stenting. *Stroke*. 2005;36(2):367-373. doi:10.1161/01.STR.0000152357.82843.9f
63. Cancel LM, Tarbell JM. The role of apoptosis in LDL transport through cultured endothelial cell monolayers. *Atherosclerosis*. 2010;208(2):335-341. doi:10.1016/j.atherosclerosis.2009.07.051
64. Lee SW, Antiga L, Steinman DA. Correlations among indicators of disturbed flow at the normal carotid bifurcation. *J Biomech Eng*. 2009;131(6):1-7. doi:10.1115/1.3127252
65. De Nisco G, Zhang P, Calò K, et al. What is needed to make low-density lipoprotein transport in human aorta computational models suitable to explore links to atherosclerosis? Impact of initial and inflow boundary conditions. *J Biomech*. 2018;68:33-42. doi:10.1016/j.jbiomech.2017.12.009
66. Chiastra C, Migliavacca F, Martínez MÁ, Malvè M. On the necessity of modelling fluid-structure interaction for stented coronary arteries. *J Mech Behav Biomed Mater*. 2014;34:217-230. doi:10.1016/j.jmbbm.2014.02.009
67. Corti A, Migliavacca F, Berceli SA, Chiastra C. Predicting 1-year in-stent restenosis in superficial femoral arteries through multiscale computational modelling. *J R Soc Interface*. 2023;20:20220876. 10.1098/rsif.2022.0876Accessed
68. Gai M, Zhu B, Chen X, et al. A prediction model based on platelet parameters, lipid levels, and angiographic characteristics to predict in-stent restenosis in coronary artery disease patients implanted with drug-eluting stents. *Lipids Health Dis*. 2021;20:118.
69. Liu H, Liu Y, Ip BYM, Ma SH. Effects of stent shape on focal hemodynamics in intracranial atherosclerotic stenosis: a simulation study with computational fluid dynamics modeling. *Front Neurol*. 2022;13:1067566. doi:10.3389/fneur.2022.1067566
70. Escuer J, Aznar I, McCormick C, Peña E, McGinty S, Martínez MA. Influence of vessel curvature and plaque composition on drug transport in the arterial wall following drug-eluting stent implantation. *Biomech Model Mechanobiol*. 2021;20(2):767-786. doi:10.1007/s10237-020-01415-3

How to cite this article: Johari NH, Menichini C, Hamady M, Xu XY. Computational modeling of low-density lipoprotein accumulation at the carotid artery bifurcation after stenting. *Int J Numer Meth Biomed Engng*. 2023; e3772. doi:10.1002/cnm.3772